AIAA AVIATION Forum
8-12 June 2026, San Diego, CA
AIAA AVIATION 2026 Forum

10.2514/6.2026-4164



# Parametric Thrust and Drag Identification from Flight Test via Energy Maneuverability

Sam A. Jaeger*
*University of Minnesota, Minneapolis, MN 55455, USA*

Martin R. Thome †
*TU Dresden, Dresden, Germany*

Demoz Gebre-Egziabher ‡
*University of Minnesota, Minneapolis, MN 55455, USA*

Maziar S. Hemati §
*University of Minnesota, Minneapolis, MN 55455, USA*

**This paper presents a method to identify both a thrust and drag model from flight test data using the concept of sensed energy maneuverability. Energy maneuverability can be sensed using acceleration and air data measurements. The proposed approach begins by determining an appropriate model structure via sparse regression. Once the parametric model structure is identified, the parameters are found using a stepwise least-squares approach. Data from flight test of a highly instrumented Ultra Stick remotely piloted aircraft is presented. Bias and scale factor errors are estimated and removed from data prior to system identification. Uncertainty analysis is performed to identify dominant sources of uncertainty as well as to quantify the uncertainty in the identified model. The identified parameters strongly agree with computational results from a blade element thrust model as well as drag estimates generated by a panel code with viscous boundary layer corrections. This energy maneuverability method provides another tool for analyzing flight test data as well as determining thrust and drag models in flight.**



## I. Introduction

Thurst and drag of an aircraft are two quantities that govern the overall vehicle performance. Range, endurance, takeoff and landing, as well as climb performance all depend on thrust and drag [1–4]. Thus, having accurate thrust and drag models of an aircraft enable engineers and pilots to utilize the vehicle to the fullest extent without compromising safety. Additionally, having these models is a critical step in model based flight control and estimator design [3, 5].

Despite the importance of thrust and drag models, determining such models prior to flight can be challenging. The propeller aerodynamics alone can be difficult to analyze analytically [1, 2, 6]. Furthermore, aircraft generally operate in speed regimes where the boundary layer that makes up the majority of the base drag is turbulent or transitions between laminar and turbulent. Knowing when the boundary layer is laminar or turbulent is critical, as skin friction drag is orders of magnitude higher for a turbulent boundary layer compared to a laminar one [7]. Finally, the propeller slipstream can interact with the base flow around the aircraft, which can alter the general thrust and drag characteristics of the aircraft.

The proliferation of unmanned aircraft in modern times poses new challenges for model-based control and estimation. Low cost airframes and hardware can introduce significant uncertainty into models developed using modern computational fluid dynamics (CFD) tools and wind-tunnel tests. In principle, modern methods in CFD can generate thrust and drag models; however, even modern day computers cannot conduct a direct numerical simulation that resolves

*Graduate Student, Department of Aerospace Engineering and Mechanics, AIAA Student Member.
†Graduate Student, Institute for Aerospace Engineering
‡Professor, Department of Aerospace Engineering and Mechanics, AIAA Fellow.
§Associate Professor, Department of Aerospace Engineering and Mechanics, AIAA Associate Fellow.

all of the length scales required to fully model turbulence around a full airplane [8]. Wind tunnel tests can also be used to guide model development; however, wind-tunnel tests are subject to tunnel test errors as well as aerodynamic scaling errors. Additionally, any sort of dynamic dependence that a full aircraft would experience in flight can be difficult to capture in a wind tunnel [9, 10]. As a result of these challenges, system identification methods are needed that can identify aircraft models via onboard instrumentation and high-speed digital acquisition systems.

Classically, in order to determine thrust from a flight test for a propeller driven aircraft, power is measured [11, 12]. This can be done by measuring the torque between the engine and the propeller and calibrating it to ground tests. Measuring torque can be cumbersome and lead to inaccuracies as a load cell needs to be placed between the engine and propeller which offsets the propeller and can cause unintended aerodynamic effects. On the other hand, drag can be calculated by knowing the thrust or given power setting [13]. Flight testing maneuvers include the speed power method, prop-feathered sinks, or incremental drag method [11]. Yet, these methods are challenged by a need for a thrust model in addition to repeated maneuvers to build a comprehensive dataset that can be used for data reduction. Indeed, most methods in aircraft system identification treat thrust as known *a priori* information [14–16]. Installation and flight effects may not be included in the provided thrust model and can, in turn, change the system identification results.

In this paper, we propose a system identification method that can identify a thrust and drag model from flight test data of a propeller driven aircraft. This is done by sensing the aircraft's change in specific energy state with respect to time, otherwise known as "energy maneuverability" [17]. Energy maneuverability has traditionally been used to calculate aircraft performance as well as to design trajectories [18–20]. In this work, we adapt energy maneuverability theory for use in a flight test context for system identification. Energy maneuverability can be calculated either from a given thrust and drag model, or alternatively from air data and acceleration measurements. In this work, we take advantage of these alternative representations of energy maneuverability to devise a system identification approach for both thrust and drag modeling based on data measured in a single flight test. The method is evaluated using flight test data from a remotely piloted fixed winged aircraft. Model validation is demonstrated by predicting energy maneuverability using the identified thrust and drag models. Additionally, model estimates generated by computation lie within expected uncertainty bounds of the identified models. These identified models can be used for future research in flight dynamics, control, and estimation.

The proposed energy maneuverability system identification method is presented in Section II. An overview of flight testing is presented in Section III. In the flight testing section, particular attention is paid to removing sensor biases and deterministic errors from the data. Finally, the system identification results along with the associated uncertainty is presented in Section IV. Conclusions follow in Section V.

## II. Parametric Thrust and Drag Identification Method

This paper uses an energy approach to formulate the flight test identification technique [11]. The key assumption in this method is knowing the functional form of the thrust and drag model. In system identification language this is known as a parametric model. To help inform the parametric model structure, aerodynamic theory and equations of motion are used to gather insight [14–16]. As such, we will first introduce the notion of energy maneuverability in Section II.A, then discuss the expected functional forms for drag and thrust modeling, respectively, in Sections II.B and II.C, before presenting the system identification approach in Section II.D.

The body fixed coordinate system used in this work is shown in Figure 1a. Additionally, the conventions for control surface deflections used in this work are also shown in Figure 1b. The overall aileron deflection reported is the average of the left and right angles: $\delta_a = \frac{\delta_{a_r} + \delta_{a_l}}{2}$. Finally, flap deflection, $\delta_f$, while not depicted, corresponds to the control surfaces inboard of the ailerons and has a positive deflection as trailing edge down.

### A. Energy Approach

Consider the total energy $E = mgh + \frac{1}{2}mV^2$ of an aircraft, where $h$ is geometric altitude, $V$ is inertial velocity, $g$ is acceleration due to gravity, and $W = mg$ is weight. The specific energy is $E_s = E/W$, or

$$E_s = h + \frac{V^2}{2g}. \tag{1}$$

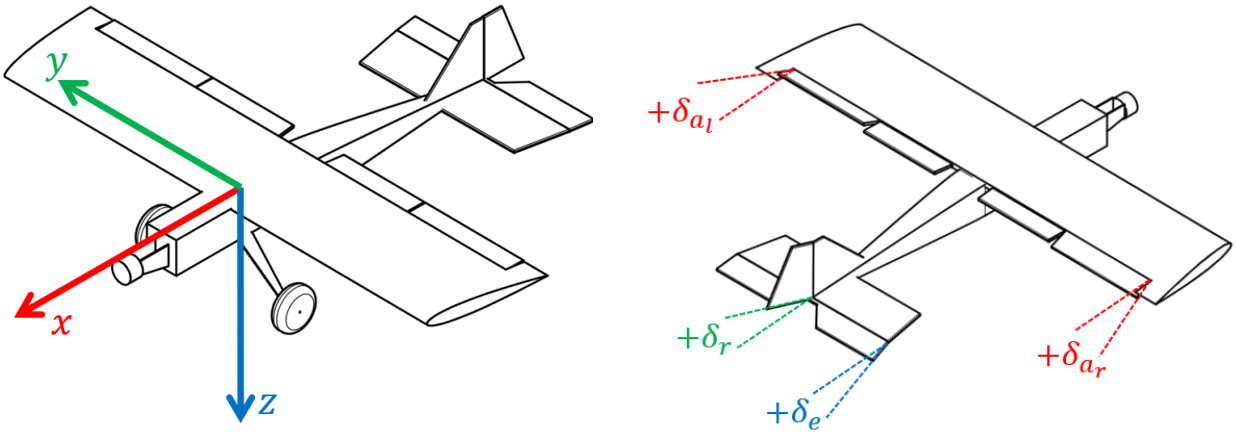


**(a) Body fixed coordinate system.** **(b) Control surface deflection conventions.**

**Fig. 1 Aircraft coordinates and control surface deflections.**

Differentiating this equation with respect to time yields energy maneuverability [17, 18] or the rate of change of specific energy $\dot{E}_s$, which is equal to the specific power $P_s$, that is

$$\dot{E}_s = \dot{h} + \frac{V\dot{V}}{g} = \frac{V(T-D)}{W} = P_s \tag{2}$$

where $T$ is thrust and $D$ is aerodynamic drag.

While energy maneuverability can be calculated by numerically differentiating altitude and airspeed time histories, this is undesirable as numerical differentiation amplifies measurement noise from the altitude and airspeed measurements. Here, we use the fact that energy maneuverability can be sensed directly from acceleration and air data measurements.

To see this, first consider the time derivative to total velocity squared,

$$\begin{aligned} \frac{d}{dt}\left(V^2\right) &= \frac{d}{dt}\left(u^2 + v^2 + w^2\right) \\ V\dot{V} &= u\dot{u} + v\dot{v} + w\dot{w}. \end{aligned} \tag{3}$$

where $u, v, w$ are velocities in the body fixed $x, y, z$ directions respectively (see Figure 1a for the coordinate system). Further, $\dot{u}, \dot{v}, \dot{w}$ can be found by rearranging the force equations of motion in terms of the acceleration of the aircraft's center of gravity (see Equation 3.52 in [15]):

$$\begin{aligned} \dot{u} &= a_x - qw + rv - g\sin\theta \\ \dot{v} &= a_y - ru + pw + g\cos\theta\sin\phi \\ \dot{w} &= a_z - pv + qu + g\cos\theta\cos\phi. \end{aligned} \tag{4}$$

where $a_x, a_y, a_z$ are the body fixed accelerations of the center of gravity in the $x, y, z$ directions respectively, $p, q, r$ are angular velocities in the body fixed $x, y, z$ directions respectively, $\phi$ is the roll attitude, and $\theta$ is the pitch attitude. Combining Equation 3 and Equation 4, substituting the relations of $v = u\tan\beta_f$, and $w = u\tan\alpha$, multiplying both sides by $1/g$, and noting that all of the angular velocity terms cancel gives,

$$\frac{V\dot{V}}{g} = \frac{u}{g}(a_x + a_y\tan\beta_f + a_z\tan\alpha) + u(-\sin\theta + \cos\theta(\tan\beta_f\sin\phi + \tan\alpha\cos\phi)) \tag{5}$$

where $\alpha$ is the angle of attack and $\beta_f$ is the flank angle. The flank angle is numerically very close to sideslip for small angles and is defined as $\beta_f \equiv \arctan(v/u)$. The time derivative of geometric altitude ($\dot{h}$) in a calm atmosphere can be written as,

$$\dot{h} = -u(-\sin\theta + \cos\theta(\tan\beta_f \sin\phi + \tan\alpha\cos\phi)). \tag{6}$$

Now combining Equation 5 and Equation 6 and noting that the attitude terms cancel gives sensed energy maneuverability:

$$\dot{E}_s = \frac{u}{g}(a_x + a_y \tan\beta_f + a_z \tan\alpha). \tag{7}$$

Equating the sensed form of energy maneuverability (Equation 7) with the analytical form of energy maneuverability (right hand side of Equation 2) yields,

$$\dot{E}_s = \frac{u}{g}(a_x + a_y \tan\beta_f + a_z \tan\alpha) = \frac{V(T-D)}{W} = P_s. \tag{8}$$

By expanding the functional form of thrust and drag, this scalar equation can be used for system identification of thrust and drag, as will be described in the ensuing sections. In order to obtain identifiable data using this method, the aircraft's energy state must be changing. Thus, maneuvers that modulate throttle and altitude help to make thrust and drag observable.

### B. Drag Model

Vehicle drag can be modeled by $D = \bar{q} S_w C_D$, where $\bar{q} = \frac{1}{2}\rho V^2$ is the dynamic pressure, $S_w$ is the wing reference area, and $C_D$ is the drag coefficient. Note that, $C_D$ is a function of the Reynolds number ($Re$), Mach number ($M$), angle of attack ($\alpha$), sideslip ($\beta$), and control surface deflections with the angle of attack being the most critical parameter influencing drag. Assuming that the vehicle operates at a Reynolds number that is on the same order of magnitude over the entire flight envelope, dependence of $Re$, and, thus, speed and altitude, can be neglected (see Appendix V.D). Additionally, for low-speed unmanned aircraft, compressibility effects are minimal and thus Mach number dependence can also be neglected. Thus, the assumed form of the drag coefficient is a summation of quadratic polynomials:

$$C_D = C_{D_0} + C_{D,\alpha}\alpha + C_{D,\alpha_2}\alpha^2 + C_{D,\beta}\beta + C_{D,\beta_2}\beta^2 + C_{D,\delta_{e2}}\delta_e^2 + C_{D,\delta_{a2}}\delta_a^2 + C_{D,\delta_{r2}}\delta_r^2 + C_{D,\delta_{f_2}}\delta_f^2. \tag{9}$$

If the control inputs over the maneuver are small or operate close to the undeflected position, then the contribution of the $C_{D,\delta}$ terms will be close to zero and the coefficients will be unobservable. Similarly, if the maneuver does not span a sufficient range of $\alpha$ or $\beta$ then the associated coefficients will also be unobservable.

The assumed form of the drag equation was informed by a combined literature survey and computational study (shown in Appendix V.D). The computational results were generated from a wing-tail model in XFLR5 which is a panel code that has viscous boundary layer corrections [21]. Parasite drag coefficient ($C_{D_0}$) estimates were also enhanced using hand calculations from [1, 22].

### C. Thrust and Propeller Theory

Insight into the functional form of a thrust model was developed from blade element theory [2, 4, 6, 11]. Blade element theory, when combined with momentum or vortex theory can predict the thrust as a function of propeller geometry and flight condition (forward velocity, rotation speed, air density, etc.). Momentum as well as vortex blade element codes were developed based on the formulations in [4, 6] (see Appendix V.C for more details). The thrust coefficient is defined as,

$$C_T = \frac{T}{\rho n^2 d^4} \tag{10}$$

where $\rho$ is the air density, $n$ is the rotational velocity of the propeller in revolutions per second, and $d$ is the diameter of the propeller. The thrust coefficient is a strong function of advance ratio, $J = \frac{V}{nd}$, and is used to combine the angular velocity of the propeller and forward flight speed into this single parameter [2, 4, 6, 11].

From blade element theory, the thrust coefficient for a conventional propeller is a polynomial function of $J$:

$$C_T = C_{T_2} J^2 + C_{T_1} J + C_{T_0}. \tag{11}$$

**D. Parametric Coefficient Fitting**

The objective of system identification is to find the coefficients in the drag and thrust polynomials in Equations 9 and 11 respectively from measured data. The thrust and drag model parameters can be organized into a column vector,

$$\boldsymbol{\theta} = [C_{T_2} \quad C_{T_1} \quad C_{T_0} \quad C_{D_0} \quad C_{D,\alpha} \quad C_{D,\alpha_2} \quad C_{D,\beta} \quad C_{D,\beta_2} \quad C_{D,\delta_{e2}} \quad C_{D,\delta_{a2}} \quad C_{D,\delta_{r2}} \quad C_{D,\delta_{f_2}}]^T \in \mathbb{R}^{K\times 1}. \tag{12}$$

These parameters can be solved for by equating the analytical form of energy maneuverability ($P_s$), which is a function of the coefficients, with the sensed form of energy maneuverability ($\dot{E}_s$):

$$P_s(\boldsymbol{\theta}) = \dot{E}_s. \tag{13}$$

The following measurements are needed for the energy maneuverability based system identification procedure: acceleration ($a_x, a_y, a_z$), airspeed in the body-fixed $x$-direction ($u$), propeller rotation rate ($n$), angle of attack ($\alpha$), flank angle ($\beta_f$), and control surface deflections ($\delta_e, \delta_a, \delta_r, \delta_f$). For low-speed, altitude, and angle of attack operations, the dynamic pressure can be approximated as the differential pressure ($\Delta p \approx \bar{q}$) sensed by a pitot tube.

At each timestep (index $k$), the parameters $\boldsymbol{\theta}$ appear linearly in the analytical form of energy maneuverability. The terms that appear in front of each of the parameters (regressors) can be assembled into a row vector of regressors denoted:

$$\boldsymbol{H}_k = \frac{V_k}{W} \begin{bmatrix} (\boldsymbol{H}_T)_k & (\boldsymbol{H}_D)_k \end{bmatrix}. \tag{14}$$

This regressor row vector can be partitioned into thrust and drag components:

$$\begin{aligned} (\boldsymbol{H}_T)_k &= \rho n^2 d^4 (\hat{V} \cdot \hat{x}) \begin{bmatrix} J^2 & J & 1 \end{bmatrix}, \\ (\boldsymbol{H}_D)_k &= -\bar{q} S_w \begin{bmatrix} 1 & \alpha & \alpha^2 & \beta & \beta^2 & \delta_e^2 & \delta_a^2 & \delta_r^2 & \delta_f^2 \end{bmatrix}. \end{aligned} \tag{15}$$

The direction of the thrust force ($\hat{x}$ unit vector) with respect to the flight path direction ($\hat{V}$ unit vector) must be accounted for in the parametric form of the equation with the dot product term:

$$\begin{aligned} \hat{V} \cdot \hat{x} &= \cos\alpha \cos\beta \\ &= \frac{\cos\alpha}{\sqrt{1 + \cos^2(\alpha) \tan^2(\beta_f)}}. \end{aligned} \tag{16}$$

The value of this term is typically near unity. For the flight test data collected, this term has an average value of 0.99. For $N$ measurements (timesteps), the row vector of regressors can be stacked into a matrix $\boldsymbol{H}$. Now Equation 13 is transformed into a linear system of equations:

$$\boldsymbol{H}\boldsymbol{\theta} = \dot{\boldsymbol{E}}_s. \tag{17}$$

where $\boldsymbol{H} \in \mathbb{R}^{N\times K}$, and $\dot{\boldsymbol{E}}_s \in \mathbb{R}^{N\times 1}$. In our work, $N$ is much larger than $K$, the problem is overdetermined and, thus, there is no unique $\boldsymbol{\theta}$. Instead, $\boldsymbol{\theta}$ is determined in a pre-defined optimal way. One way of solving for $\boldsymbol{\theta}$ is by minimizing the error between $\boldsymbol{H}\boldsymbol{\theta}$ and $\dot{\boldsymbol{E}}_s$ in a least-squares sense [14, 23]:

$$\min_{\boldsymbol{\theta}} ||\boldsymbol{H}\boldsymbol{\theta} - \dot{\boldsymbol{E}}_s||_2^2. \tag{18}$$

Using this optimization problem as the basis for system identification, a two step solution approach is proposed. First the model structure is identified in $\boldsymbol{\theta}$. Then the model is refined by solving Equation 18.

*1. Model Structure Identification*

The first method used to estimate the thrust and drag model parameters $\boldsymbol{\theta}$ is to minimize a cost function, $J_c$, that is a function of $\boldsymbol{H}, \boldsymbol{\theta}, \dot{\boldsymbol{E}}_s$ subject to bounds on $\boldsymbol{\theta}$. The optimization problem chosen to solve this problem is:

$$\begin{aligned} &\min_{\boldsymbol{\theta}} \ ||\boldsymbol{H}\boldsymbol{\theta} - \dot{\boldsymbol{E}}_s||_2^2 + \kappa||\boldsymbol{\theta}||_1 \\ &subject\ to \quad \boldsymbol{\theta}_L \leq \boldsymbol{\theta} \leq \boldsymbol{\theta}_U, \end{aligned} \tag{19}$$

where $\kappa \geq 0$ is a tuneable hyperparameter that promotes sparsity in the solution $\boldsymbol{\theta}^*$. $\boldsymbol{\theta^*}$ denotes the solution corresponding to the minimum $J_c^*$. The 2-norm in the objective function minimizes the error between the measured data and the fitted model. The 1-norm of $\boldsymbol{\theta}$ enhances sparsity in the solution which helps to find the relative importance of each of the fitted parameters. This is helpful in determining model structure. The bounds on $\boldsymbol{\theta}$ help to ensure that the optimization converges to a physical solution. For instance, drag must be positive. Additionally, thrust should decrease with increasing advance ratio for a fixed pitch propeller. The optimization problem 19 is convex and can be solved efficiently by off the shelf convex optimization solvers such as Mosek [24].

*2. Model Refinement*

Equation 19 has an analytical solution when $\kappa = 0$ and the problem is unconstrained [23, 25]. This analytical solution is a standard least-squares whose solution is given by,

$$\boldsymbol{\theta}_{LS}^* = \left(\boldsymbol{H}^T\boldsymbol{H}\right)^{-1}\boldsymbol{H}^T\dot{\boldsymbol{E}}_s. \tag{20}$$

While this linear algebra solution is straightforward to implement, it is prone to overfitting errors if the model structure is not well known or if there is significant measurement noise [14, 15]. Furthermore there is no guarantee that the solution will be physically meaningful since there are no constraints on $\boldsymbol{\theta}$. Nonphysical solutions from least-squares could be due to a wrong model form, significant measurement noise in $\boldsymbol{H}$ or $\dot{\boldsymbol{E}}_s$, or dynamically/kinematically inconsistent data. To mitigate the impact of these factors, first a low pass filter is applied to all of the raw input signals. Static errors were removed from these filtered signals and were also checked for consistency as described in Section III. A model structure study was performed by solving Equation 19 for a range of $\kappa$. Once the model structure was determined, Equation 20 was used to solve for the parameters.

## III. Flight Testing of an Ultra Stick Remotely Piloted Aircraft

Flight testing was conducted on a highly instrumented Ultra Stick RC aircraft. The Ultra Stick was chosen as a platform due to its low cost nature and its extensive use in historical flight dynamics research [9, 26, 27]. Figure 2 shows the current Ultra Stick in flying configuration.

**Fig. 2 Ultra Stick flight test aircraft from the University of Minnesota UAV lab. This Ultra Stick airframe, known as IBIS, is heavily instrumented as discussed in Section III.A.**

The configuration of the Ultra Stick was modified from the original off the shelf condition by converting the power system from a gas power plant to an electric motor with a fixed pitch propeller. Additionally, the stock tailwheel was replaced with a modified one to improve the ground handling qualities due the additional weight of the sensor suite. A summary of the aircraft's flight configuration is shown in Table 2.

**Table 2 Ultra Stick geometry and weight.**

| Quantity | Value | Description / Manufacturer |
|---|---|---|
| $W$ | 20.17 $lb$ | Weight |
| $S_w$ | 7.91 $ft^2$ | Wing Area |
| $\bar{c}$ | 1.25 $ft$ | Mean Aerodynamic Chord |
| $b_w$ | 6.33 $ft$ | Wingspan |
| $x_{cg}$ | 1.125 $ft$ | x CG Location Aft of the Firewall |
| $x_{mw}$ | 0.666 $ft$ | x Location of the Main Wing Leading Edge Aft of the Firewall |
| $x_{ht}$ | 3.708 $ft$ | x Location of the Horizontal Tail Leading Edge Aft of the Firewall |
| $x_{vt}$ | 3.375 $ft$ | x Location of the Vertical Tail Leading Edge aft of the Firewall |
| $S_t$ | 2.06 $ft^2$ | Horizontal Tail Area |
| $S_v$ | 0.718 $ft^2$ | Vertical Tail Area |
| $Propeller$ | $16 \times 8E$ | APC |
| $ESC$ | SPMXAE 1120 HV 120 Amp | Spektrum |
| $Motor$ | Power 110 | E-Flite |
| $Battery$ | 12S, 10000 mAh, 100C | Spektrum |

Flight tests were conducted on calm days at the Anoka County RC flying field. A position ground track during a test flight is shown in Figure 3.


**Fig. 3 GPS ground track position of a flight test.**

Air density was estimated using the ideal gas law ($\rho = p/RT$). Ambient temperature and pressure data was found by taking temperature readings at the field and recording the altimeter setting at several nearby airports with AWOS stations. A hand held anemometer was used to record the wind direction and speed. A summary of weather recordings for the flight test day are shown in Table 3.

**Table 3 Weather at the Anoka County RC field on 10/30/25.**

| Time | Temperature | Wind Direction | Wind Magnitude | KANE Altimeter | KCBG Altimeter |
|---|---|---|---|---|---|
| 9:36 | 46.4 F | 000 | 0 ft/s | 30.01" Hg | 29.99" Hg |
| 11:51 | 42 F | 000 | 0 ft/s | 30.00" Hg | 30.00" Hg |
| 12:45 | 44.1 F | 300 | 4.5 ft/s | 29.99" Hg | 29.98" Hg |

The ambient air density used for all calculations was set to $\rho = 0.002361\ slugs/ft^3$. The subsequent subsections overview the data acquisition system, individual measured variables for a representative 12 second throttle doublet maneuver, as well as steps taken to estimate deterministic sensor bias and scale factor errors.



### A. Sensor Suite Overview and Data Collection

The Ultra Stick airframe has been highly instrumented to carry a suite of sensors which are summarized in Table 4. These include the Honeywell n580 Inertial Navigator, and the Bolder Flight Systems Flight Management Unit for Research (FMU-R). The FMU-R serves as a flight computer and logs data from the air data pressure sensors, potentiometers, and a back-EMF propeller RPM (revolutions per minute) sensor.

**Table 4 Sensors on IBIS.**

| Sensor | Measured Quantities |
|---|---|
| n580 | $a_x, a_y, a_z, p, q, r, V_n, V_e, V_d, latitude, longitude, altitude, \phi, \theta, \psi$ |
| FMU-R | $a_x, a_y, a_z, p, q, r, V_n, V_e, V_d, latitude, longitude, altitude$ |
| Air Data | $p_{static}, \Delta p$ |
| Potentiometers | $\alpha, \beta_f, \delta_e, \delta_a, \delta_r, \delta_f$ |
| RPM back-EMF | $RPM$ |

The FMU-R serves as the main data processing unit and has its own inertial measurement unit (IMU) and global positioning system (GPS) module. IMU, GPS, air data, voltages from potentiometers, and RPM values are all recorded on the FMU-R. Angle of attack and flank angle (sideslip) information are determined from potentiometer voltages on the wingtip air data probes. A calibration is used to determine the physical angle of attack and sideslip. Additionally, the control surfaces are also instrumented with potentiometers and record deflection angles a similar way. The propeller RPM is recorded by measuring the induced voltage from the rotation of the rotor in the motor phases - called back-EMF. The back-EMF pulses are recorded and timestamped by the FMU-R.

Prior to using the data for system identification, all of the raw signals were checked for instrumentation errors and transformed to the traditional flight dynamic definitions [14, 15]. Biases were estimated and removed from the data either using estimates generated prior to takeoff or in flight data. Data consistency was established by reconstructing air data velocities and attitudes via numerical integration of accelerometers and rate gyros and comparing measured to reconstructed solutions. The air data state can be reconstructed by integrating the three $\dot{u}, \dot{v}, \dot{w}$ equations in Equation 4. Air data measurements at a particular time are given as an initial condition and the measured acceleration, angular velocity, and attitude solutions are used as time varying inputs to this differential equation [15].

In addition to static errors, all of the raw measurements are corrupted by high frequency noise. This noise can propagate into the identified model if not treated properly, especially if the measurements are used in the regressor matrix, $\boldsymbol{H}$ [14, 15, 28, 29]. In order to combat this, a digital low pass filter is applied to the raw data. A Simpson 15 point digital filter from [14] has been used as the low pass digital filter in this study:

$$y_k = \frac{1}{320}(-3z_{k-7} - 6z_{k-6} - 5z_{k-5} + 3z_{k-4} + 21z_{k-3} + 46z_{k-2} + 67z_{k-1} + 74z_k + 67z_{k+1} + 46z_{k+2} + 21z_{k+3} + 3z_{k+4} - 5z_{k+5} - 6z_{k+6} - 3z_{k+7}). \tag{21}$$

where $z_k$ is the raw measurement and $y_k$ is the filtered measurement for a particular timestep. The Simpson filter is a weighted moving average filter and does not introduce time lag due to its symmetrical nature [14]. For the 100 $Hz$ sampling rate of the n580 and FMU-R, the 15 point Simpson filter has a fixed cutoff frequency of $\approx 10$ $Hz$ (using a $-3$ $dB$ threshold). Because the thrust and drag dynamics that are sought to be identified are much lower frequency than the measurement noise ($< 5$ $Hz$ [14, 15]), data removal is expected to be minimal in this process. Optimal Fourier smoothing [15, 30] was investigated but not ultimately used due to the increase in computation time as well as the necessity of user input to set an appropriate cutoff frequency that does not discard dynamics.

*1. GPS Synchronization*

The Honeywell n580 Inertial Navigator operates independently and does not interface directly with the FMU-R. Consequently, measurements from the n580 are not inherently synchronized with those from the FMU-R, such as potentiometer and air data. Any clock drift between the FMU-R and the n580 could complicate efforts to align their respective datasets. To address this challenge, GPS time serves as a common temporal reference. The n580 is configured to record data that is valid at its GPS time tag. To achieve similar synchronization on the FMU-R, software was developed to eliminate FMU-R clock drift by measuring its GPS receiver latency and continuously aligning its internal time with GPS time.

GPS latency is the delay between the moment a GPS receiver acquires satellite signals and computes the position, velocity, and time solution (PVT) and the moment when the PVT information becomes available to the FMU-R flight computer. This latency arises mainly from processing time inside the GPS receiver, as well as additional delays in communication and data handling. As a result, PVT data supplied to the FMU-R typically describe the state that occurred approximately 50 to 100 milliseconds earlier.

To compensate for this latency, the Pulse Per Second (PPS) signal provided by the GPS receiver is utilized. The PPS signal is a highly accurate electrical timing pulse generated once per second and is synchronized with the start of each GPS time second. Its rising edge marks the beginning of a new GPS time second and is detected and timestamped by the FMU-R. When the FMU-R detects the PPS signal's rising edge, it takes the latest GPS time reported and rounds it up to the next full second, identifying this as the true current GPS time. Between PPS pulses, the FMU-R's internal clock is used to extrapolate time tags for sensor data. Each time a new PPS pulse is detected, the synchronization process is repeated, realigning the FMU-R's internal timing with GPS time. To obtain synchronized FMU-R timestamps $t_{sync}$, the following equation is used:

$$t_{sync} = tow_{PPS} + t_{FMUR} - t_{PPS} \tag{22}$$

Here, $tow_{PPS}$ is the GPS TOW when the PPS rising edge is detected, rounded up to the next full second, $t_{FMUR}$ is the current time value of the FMU-R's internal clock, and $t_{PPS}$ is the FMU-R's timestamp of the last PPS rising edge. This synchronization approach is illustrated in Figure 4. Note, that $t_{sync}$ is in the domain of GPS TOW and provides timestamps directly comparable to the n580 GPS time tag.

By applying this procedure, the FMU-R's internal time is realigned with GPS time every second. As a result, the FMU-R clock is only relied upon for one second, and clock drift becomes insignificant.

The implementation of this method relies on software-generated timestamps, which make it straightforward to implement. Although software interrupts can introduce slight delays, on the FMU-R these are limited to the nanosecond scale and are therefore sufficiently precise for the needs of this project. In cases where greater timing precision is necessary, hardware-based timestamping, as outlined in [31], is recommended to minimize software-induced delays.

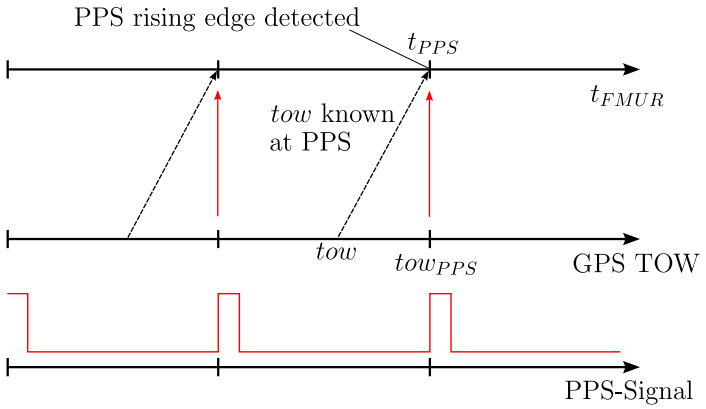


**Fig. 4 FMU-R GPS synchronization utilizing the PPS signal from the GPS receiver.**



### B. Pitot - Static System Calibration

Before using static and differential pressure data to calculate airspeeds, scale factor and bias errors were found and removed from the data.

First, the static pressure bias was estimated by using the altitude (MSL) position solution from the n580 ($h$) and the reported altimeter setting at a local airport. Ambient pressure ($p$) was estimated via the standard atmosphere pressure relation in the Troposphere [32]:

$$p = p_{SL}(1 - (6.87559 \cdot 10^{-6})h)^{5.2559} \tag{23}$$

where $p_{SL}$ is the altimeter setting reported at the local airport (which is corrected to sea level) and $h$ is measured in feet. Using this estimated pressure as ground truth, the static pressure bias was calculated using least-squares which is the average error between the estimated pressure and the measured static pressure. Scale factor errors were found to be negligible for the static pressure sensor.

Assuming there is no wind (data was collected on a calm day), true airspeed as well as angle of attack and slideslip can be found synthetically using the n580 inertial velocity as well as attitude solutions. The inertial velocity solution is composed of north-east-down velocity $(V_n, V_e, V_d)$ and the attitude solution is composed of the traditional roll-pitch-yaw Euler angles $(\phi, \theta, \psi)$. This synthetic solution was used to calibrate the airspeed measurements made by the pitot-static system as well as validate the wingtip angle of attack and sideslip probe measurements. The north-east-down velocity solution generated by the n580 can be transformed into body fixed velocities by computing the inverse of the direction cosine attitude solution matrix at every timestep (using a calm wind assumption). The direction cosine matrix is an orthogonal matrix and its inverse is a transpose:

$$\begin{bmatrix} u_{n580} \\ v_{n580} \\ w_{n580} \end{bmatrix} = \begin{bmatrix} \cos\theta\cos\psi & \sin\phi\sin\theta\cos\psi - \cos\phi\sin\psi & \cos\phi\sin\theta\cos\psi + \sin\phi\sin\psi \\ \cos\theta\sin\psi & \sin\phi\sin\theta\sin\psi + \cos\phi\cos\psi & \cos\phi\sin\theta\sin\psi - \sin\phi\cos\psi \\ -\sin\theta & \sin\phi\cos\theta & \cos\phi\cos\theta \end{bmatrix}^T \begin{bmatrix} V_n \\ V_e \\ V_d \end{bmatrix}. \tag{24}$$

Next airspeed was calculated using the differential pressure measurements coming from the pitot tube. The pitot tube is assumed to be aligned directly in the body fixed $x$ direction which corresponds to the $u$ airspeed. A pitot-static bias and scale factor error $(b_{\Delta p}, \lambda_{\Delta p})$ was estimated by comparing an estimated differential pressure from n580 inertial velocity solution with the measured differential pressure (wind was calm while collecting this data). Calibrated airspeed [32] follows Equation 25:

$$u_c = \sqrt{\left(\frac{7p_{SL}}{\rho_{SL}}\right)\left(\left(\frac{\Delta p}{p_{SL}} + 1\right)^{2/7} - 1\right)} \tag{25}$$

where $\rho_{SL}$ and $p_{SL}$ is a fixed density and pressure at sea level. Solving Equation 25 for $\Delta p$ gives,

$$\Delta p_{n580} = p_{SL}\left(\frac{\rho_{SL}}{7p_{SL}}u_{n580}^2 + 1\right)^{7/2} - p_{SL}. \tag{26}$$

Using $\Delta p_{n580}$ as the ground truth, the scale and bias errors in the differential pressure sensor can be estimated. A general measurement equation for the differential pressure (neglecting random errors) is,

$$\Delta p = (1 + \lambda_{\Delta p})\Delta p_{n580} + b_{\Delta p}. \tag{27}$$

For $N$ measurements this can be formulated in a matrix:

$$\begin{bmatrix} \Delta p_{n580_1} & 1 \\ \Delta p_{n580_2} & 1 \\ \vdots & \vdots \\ \Delta p_{n580_N} & 1 \end{bmatrix} \begin{bmatrix} (1 + \lambda_{\Delta_p}) \\ b_{\Delta_p} \end{bmatrix} = \begin{bmatrix} \Delta p_1 \\ \Delta p_2 \\ \vdots \\ \Delta p_N \end{bmatrix}. \tag{28}$$

This matrix equation can be solved using least-squares. Nonstandard temperature and pressure effects were found to have a minimal effect on the calibration results. Thus, calibrated airspeed (rather than true airspeed) was used in system identification. This was done in order to minimize the propagation of additional sources of sensor error into the identified model. The resulting corrected static pressure as well as calibrated differential pressure time histories during a throttle step maneuver are shown in Figure 5.

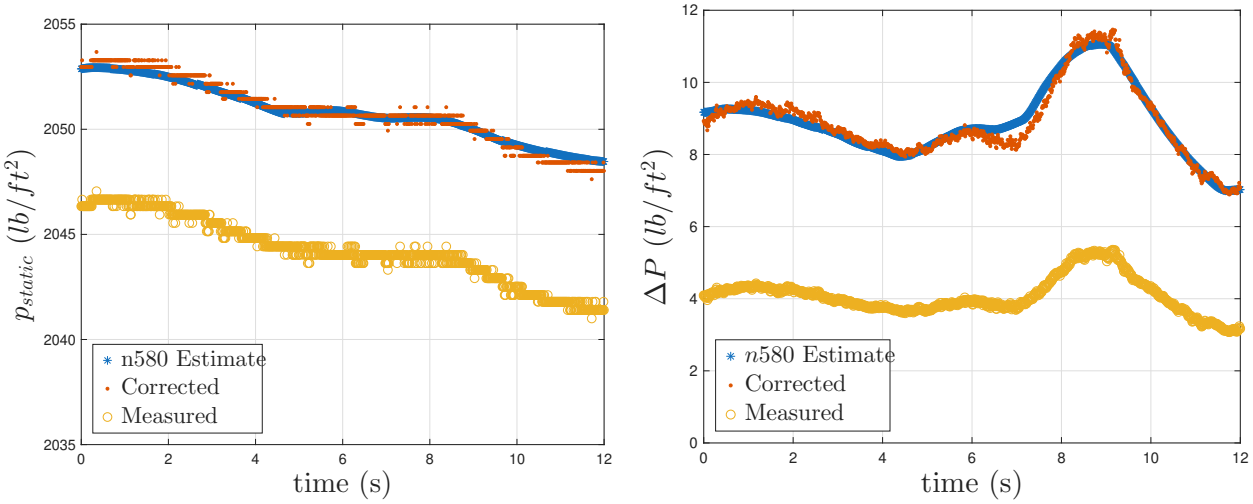


**(a) Static pressure time history. The corrected values include bias corrections.**

**(b) Differential pressure time history. The corrected values includes bias and scale factor corrections.**

**Fig. 5 Static pressure and differential pressure time histories during a throttle step maneuver.**

### C. Air Data Angles

From the n580 body fixed velocity solution, $\alpha$ and $\beta_f$ can be found via the relations [4, 15]:

$$\begin{aligned} \beta_f &= \arctan(v/u) \\ \alpha &= \arctan(w/u). \end{aligned} \tag{29}$$

Sideslip can be found via $\beta = \tan^{-1}\left(\cos\alpha \tan\beta_f\right)$. The resulting angle of attack and flank angle time histories from the synthetic n580 solution as well as the measured probe angles are shown in Figure 6. Since the air data probes as well are located at the wingtips, the measured angles and velocities are translated to the center of gravity via the procedure documented in Appendix V.A.

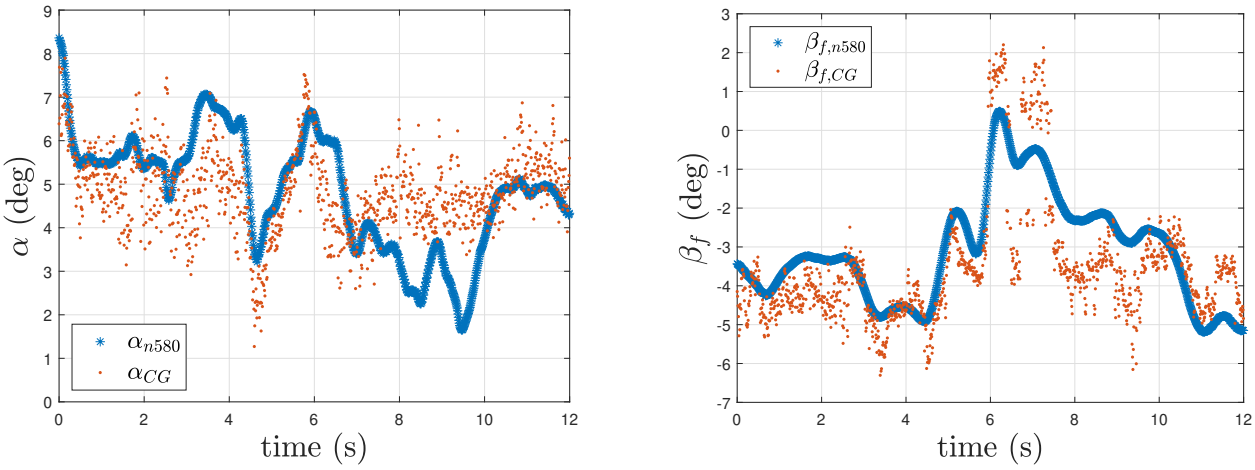


**(a) Angle of attack time history.** **(b) Flank angle time history.**

**Fig. 6 Air data angles from the synthetic n580 solution as well as the air data probes during a throttle doublet.**

For the most part, the synthetic air data solution matches the probe measurements. Certain sections of the time histories do not match which is likely due to dynamics associated with the probe during the maneuver.

### D. Inertial Measurements: Acceleration and Angular Velocity

Acceleration and angular velocity ($p, q, r$ in the $x, y, z$ body fixed frame) are two critical quantities that both the FMU-R as well as n580 report. In the case of acceleration, these measurements are directly used in the calculation of energy maneuverability. Angular rate measurements are used to translate air data measurements to the center of gravity of the aircraft. Extensive vibration was observed in the inertial measurements which is likely a result of the electric motor. The motor operates at a much higher frequency than the sampling rate of either the n580 or FMU-R which prevents identification and separation of vibration and sensor noise. The digital low pass filter in Equation 21 was employed to mitigate the effects of this noise in the acceleration measurements. Additionally, bias errors were estimated using a portion of data when the aircraft was not moving and were removed from the dataset. The bias errors from the n580 were found to be negligible compared to the bias errors of the FMU-R's IMU. Given that the IMU in the n580 is a tactical grade sensor and those in the FMU-R is a consumer/industrial grade, the noise characteristics of the n580 are expected and were found to be much lower than the FMU-R [33, 34]. Finally, the physical offset from the vehicle's center of gravity to the n580 was found to be a negligible effect as the n580 is mounted within a few inches of the center of gravity. For these reasons, the filtered n580 measurements are used in the system identification procedure in order to eliminate the possible propagation of errors from the FMU-R's IMU. Time histories of the n580 acceleration measurements are shown in Figure 7.

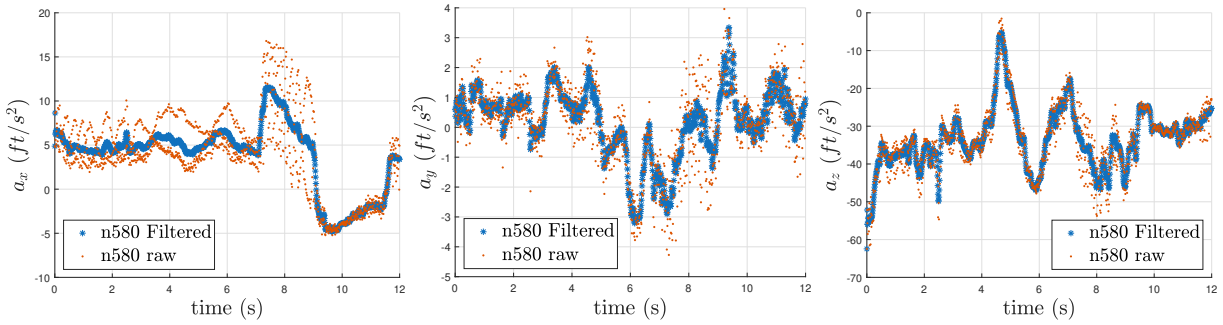


**(a) Body fixed $x$ acceleration.** **(b) Body fixed $y$ acceleration.** **(c) Body fixed $z$ acceleration.**

**Fig. 7 n580 acceleration time histories during a throttle doublet maneuver. Low pass filtering was applied to remove noise primarily coming from vibration.**

## E. Control Surface Deflections

The control surface deflections were measured via potentiometers. These potentiometers measure voltages and are then translated into deflection angles via a calibration curve. The calibration was conducted prior to flight using a wireless accelerometer that could measure the angle between the gravity vector and the control surface deflection. Representative time histories of the elevator, aileron, and rudder are shown in Figure 8.

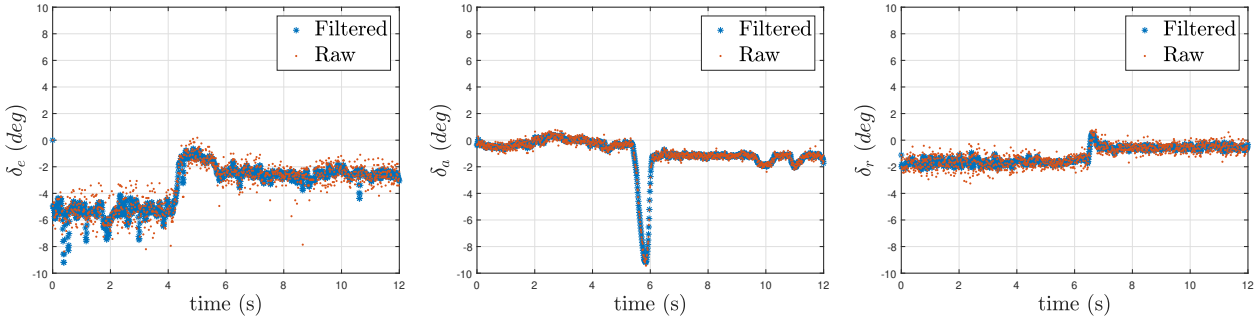


**(a) Elevator deflection time history.** **(b) Aileron deflection time history.** **(c) Rudder deflection time history.**

**Fig. 8 Control surface deflection time histories during a throttle doublet maneuver.**

## F. RPM and Advance Ratio

RPM was measured using a back EMF sensor that was soldered onto two of the motor phase wires. Significant electrical noise was seen in the data; the cause of this is unknown. RPM measurements from the back EMF sensor were checked against measurements taken using a photo tachometer prior to flight to ensure RPM measurements were unbiased. RPM measurements are also needed to calculate advance ratio. The advance ratio was calculated using the calibrated airspeed found after scale factor and bias errors were removed. Representative time histories of the RPM and advance ratio are shown in Figure 9.

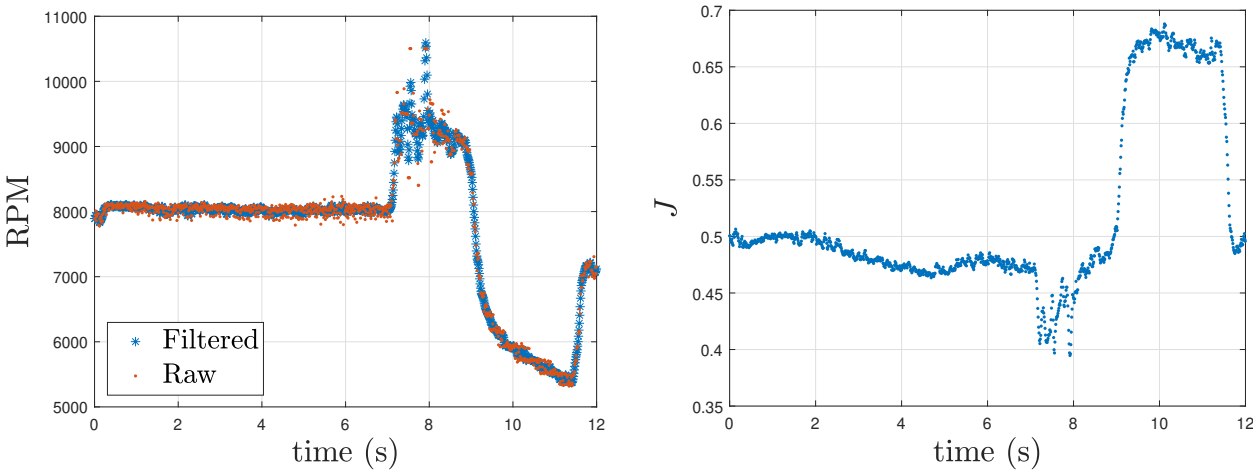


**(a) RPM time history.** **(b) Advance ratio time history.**

**Fig. 9 RPM and advance ratio time histories during a throttle doublet.**

# IV. Thrust and Drag System Identification Flight Test Results

The system identification process that has been undertaken in this work has three general steps:

1) filtering of data and propagation of uncertainty,
2) model form study,
3) least-squares solution.

Because the optimization and linear algebra approaches to the system identification are prone to develop errors in the estimated parameters when there is measurement noise, appropriate low pass filtering techniques are applied to remove random errors prior to identification. Sensor noise statistics are estimated by comparing the low pass filtered signal with the measured signals. These statistics are then propagated into the sensed energy maneuverability function as well as the identified model. A model formulation study is completed to identify dominant terms in the proposed model structure. This is especially important if using linear algebra approaches as least-squares can give nonphysical results if an incorrect model form is assumed. Once a model form is identified, least-squares is used to solve for the identified parameters.



## A. Energy Maneuverability Uncertainty

Sensor readings used in the system identification process contain random errors. These propagate into the sensed energy maneuverability function and then also into the identified model. An uncertainty analysis is performed to:

1) give an indication of the dominant uncertainty contributions from each of the sensor channels,
2) find how uncertain the identified thrust and drag model is.

Once the bias and scale factor errors are removed from the individual time histories, a sensed quantity is assumed to have random noise that is added to the measurement of the form of:

$$z = y + v \tag{30}$$

where $z$ is the measurement, $y$ is the true value, and $v$ is uncorrelated noise with an expected value of zero and a variance of $\sigma^2$ ($\mathbb{E}[v] = 0, \mathbb{E}[v^2] = \sigma^2$). These individual sensor variances are estimated by taking the variance of the raw measurement signal minus the low pass filtered signal ($\mathbb{E}[(z-y)^2]$). Using these estimates, the overall uncertainty in the sensed energy maneuverability can be found by propagating the individual sensor noise statistics using a first order Taylor series:

$$\sigma_{\dot{E}_s} = \sum_{j=1}^{N_{sensor}} \sqrt{\left(\sigma_{z_j}\left(\frac{\partial \dot{E}_s}{\partial y_j}\right)\right)^2}. \tag{31}$$

The sensitivities and the estimated standard deviations are summarized in Table 5. The estimated standard deviations are compared with a bench top experiment where a multi hour time history was taken while the aircraft was stationary in the lab. The effect of having an accurate model of gravity was also analyzed by estimating the uncertainty in the acceleration due to gravity with two significant digits.

**Table 5 Sensitivities and noise properties.**

| $z_j$ | $(\sigma_{z_j})_{estimated}$ | $(\sigma_{z_j})_{bench}$ | $\frac{\partial \dot{E}_s}{\partial y_j}$ |
|---|---|---|---|
| $\Delta p$ | 0.06324 $(lb/ft^2)$ | 0.0032 $(lb/ft^2)$ | $\frac{\partial \dot{E}_s}{\partial u_c}\frac{\partial u_c}{\partial(\Delta p)} = \frac{a_x + a_y \tan\beta_f + a_z \tan\alpha}{g u_c \rho_{SL}\left(1+\frac{\Delta p}{P_{SL}}\right)^{5/7}}$ |
| $a_x$ | 2.6358 $(ft/s^2)$ | 0.0392 $(ft/s^2)$ | $\frac{\partial \dot{E}_s}{\partial a_x} = u_c/g$ |
| $a_y$ | 0.8532 $(ft/s^2)$ | 0.0365 $(ft/s^2)$ | $\frac{\partial \dot{E}_s}{\partial a_y} = \frac{u_c}{g}\tan\beta_f$ |
| $a_z$ | 3.1317 $(ft/s^2)$ | 0.057 $(ft/s^2)$ | $\frac{\partial \dot{E}_s}{\partial a_z} = \frac{u_c}{g}\tan\alpha$ |
| $\alpha$ | 0.4035 $(deg)$ | 0.1157 $(deg)$ | $\frac{\partial \dot{E}_s}{\partial \alpha} = \frac{u_c}{g}(\sec^2\alpha)a_z$ |
| $\beta_f$ | 0.2931 $(deg)$ | 0.0455 $(deg)$ | $\frac{\partial \dot{E}_s}{\partial \beta_f} = \frac{u_c}{g}(\sec^2\beta_f)a_y$ |
| $g$ | 0.01 $(ft/s^2)$ | 0.01 $(ft/s^2)$ | $\frac{\partial \dot{E}_s}{\partial g} = -\frac{u_c}{g^2}(a_x + a_y\tan\beta_f + a_z\tan\alpha)$ |

The noise properties found in the lab were much lower than the estimated noise properties in flight likely due to vibration and other flight related process noise. The individual variables contributing to the overall energy maneuverability uncertainty can be plotted as a function of time as shown in Figure 10. These are computed by multiplying the standard deviation by the estimated sensitivity of the variable and squaring the product: $\delta_j^2 = \left(\sigma_{z_j}\left(\frac{\partial \dot{E}_s}{\partial y_j}\right)\right)^2$.

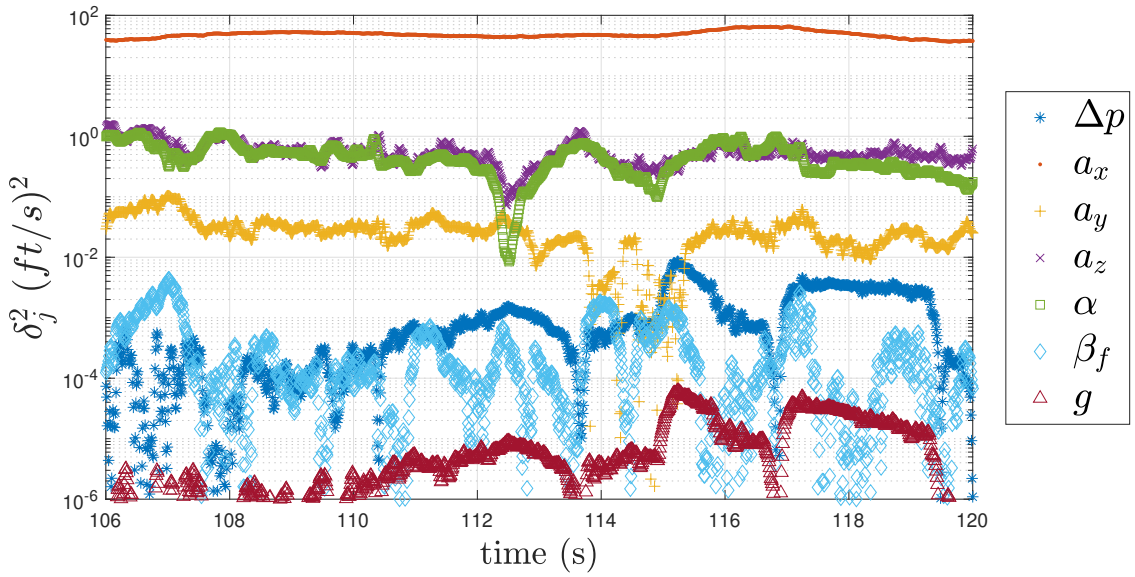


**Fig. 10 Uncertainty contribution from each of the sensed quantities in energy maneuverability during a throttle doublet.**

Figure 10 shows that by far the sensor that contributes the most to the overall energy maneuverability is acceleration in the $x$ direction. Secondary importance is angle of attack and $z$ acceleration measurements. The high uncertainty in the acceleration measurements are due to significant vibration observed in the acceleration data (see Figures 7a, 7b, 7c). The effect of uncertainty in gravity in energy maneuverability measurements was found to be insignificant compared to the other measurements.

Based on this uncertainty model of energy maneuverability, the measurement covariance matrix, $\boldsymbol{R}_{EM}$, can be formulated as a diagonal matrix of the energy maneuverability uncertainty squared:

$$\boldsymbol{R}_{EM} = diag((\sigma_{\dot{E}_s})_k^2). \tag{32}$$

Using this measurement covariance matrix, the identified model model covariance matrix, $\boldsymbol{Q}$, can be calculated via:

$$\boldsymbol{Q} = \left(\boldsymbol{H}^T \boldsymbol{R}_{EM}^{-1} \boldsymbol{H}\right)^{-1}. \tag{33}$$

Equation 33 corresponds to the covariance matrix generated by weighted least-squares with a weighting matrix $\boldsymbol{R}_{EM}^{-1}$ [15]. The diagonal of $\boldsymbol{Q}$ represent the estimated variances of the identified parametric model.

The covariances identified by Equation 33, are consistent with the covariances generated an estimated least-squares covariance matrix described in [14, 15]:

$$\boldsymbol{Q}_{est.} = \frac{1}{N(N-K)}\left(\frac{1}{N}\boldsymbol{H}^T\boldsymbol{H}\right)^{-1} ||\dot{\boldsymbol{E}}_s - \boldsymbol{H}\boldsymbol{\theta}^*||_2^2 \tag{34}$$

where $N$ is the number of data points and $K$ are the number of parameters that are fitted.

### B. Thrust Identification

The thrust and drag identification are separated into subsequent steps due to the limited amount of maneuvers that span an adequate range of advance ratios. The drag model structure was set during thrust identification to only the $C_{D_0}$

and $C_{D,\alpha_2}$ terms. Furthermore, because of the lack of low advance ratio data ($J < 0.2$), the static thrust coefficient was also fixed to a value of $C_{T_0} = 0.0892$. This value was generated using blade-element-vortex theory and is consistent with static thrust results. Appendix V.B compares the static thrust coefficient with blade-element-vortex theory as well as the published dataset from [35]. Without fixing static thrust, flight identified results for $C_{T_0}$ were found to be much lower ($C_{T_0} \approx 0.7$) compared to theory and ground testing. Furthermore, the identification cannot distinguish between $C_{T_1}$ and $C_{T_2}$ because the available thrust data behaves in a linear fashion with respect to advance ratio. Thrust was identified using a throttle step maneuver. The advance ratio associated with this maneuver spans a range of between .4 and .7 and is shown in Figure 9b. The identified results are summarized in Table 6. The identified model is compared with blade-element-momentum (BEM), blade-element-vortex (BEV), and a wind tunnel dataset from [35]. The last column of Table 6 include estimated uncertainties in the form of standard deviations (square root of the associated diagonal entry of Equation 33). The uncertainty in the static thrust coefficient is modeled by the variation observed in the static thrust data with respect to RPM.

**Table 6 Identified parametric thrust coefficient model.**

| $C_i$ | Blade-Element-Momentum | Blade-Element-Vortex | Data from [35] - 6000 RPM | Flight | $\sigma_i$ |
|---|---|---|---|---|---|
| $C_{T_2}$ | -0.0589 | -0.0617 | -0.1881 | -0.13512 | 0.0117 |
| $C_{T_1}$ | -0.0954 | -0.0941 | -0.0357 | -0.05031 | 0.00933 |
| $C_{T_0}$ | 0.0898 | 0.0892 | 0.1007 | No ID | 0.0053 |

A plot of the identified thrust coefficient model versus advance ratio for is shown in Figure 11. A $\pm 3\sigma$ bound is also plotted around the identified thrust model from flight.

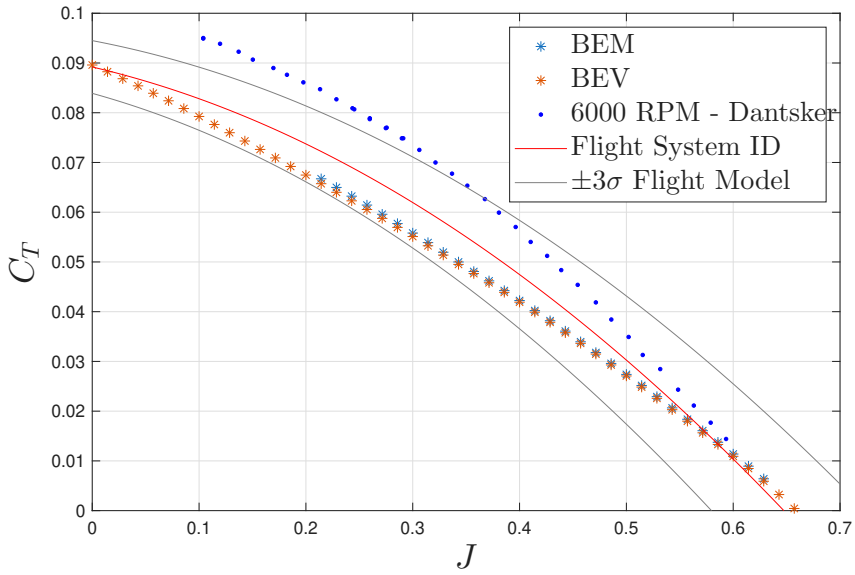


**Fig. 11 Thrust coefficient versus advance ratio results from computation, flight test, and [35] for the APC 16x8E propeller.**

The identified thrust coefficient model agrees very closely with the computational and published experimental results for the advance ratios that were obtained in flight ($0.4 < J < 0.7$). The computational results and the majority of the results from [35] stay within the estimated $\pm 3\sigma$ uncertainty bound. The uncertainty bound indicates that either the model from [35] or blade element theory could be used to model thrust in advance ratios $J > 0.4$. The mismatch between computation and [35] could be due to the fact that the blade element code uses airfoil cross section data for very high Reynolds numbers ($Re \approx 1e6$) which correspond to RPMs greater than the 6000 RPM data in [35]. Since the measured RPM was well beyond 6000 for the majority of the flight, the higher RPM is hypothesized as the reason why the flight identified model matches computation more closely than [35].

## C. Drag Model Form Study

In order to better understand the dominant terms in $\boldsymbol{\theta}$, Equation 19 can be solved iteratively for increasing values of a tuneable hyperparameter $\kappa$. For larger values of $\kappa$, a more sparse solution is desired. Thus, the effect of dominant terms on the cost function will increase when this sparsity parameter is also increased. The difference between the measured energy maneuverability and each of the columns of the $\boldsymbol{H}$ matrix can be monitored as a function of $\kappa$:

$$J_{c_i,\kappa} = ||\boldsymbol{H}_i\theta_i(\kappa) - \dot{\boldsymbol{E}}_s||_2. \tag{35}$$

The square is removed for simplicity. The variation of $J_{c_i,\kappa}$ (column error for a given $\kappa$ divided by the column error when $\kappa = 0$) is plotted versus $\kappa$ in Figure 12. A value of 1 corresponds to a column error for a given $\kappa$ as being the same as the column error as the least-squares solution. A value of 1 indicates that the parameter doesn't change the fit significantly due to either insufficient data or the parameter isn't significant in the model. An increasing value signals that a particular parameter has a strong effect on fitting the data. Finally, a decreasing value shows that the parameter isn't needed to model the data. Variables that significantly affect drag (called primary variables) are identified in Figure 12a and variables that don't have an as strong effect on drag (secondary variables) are shown in Figure 12b.

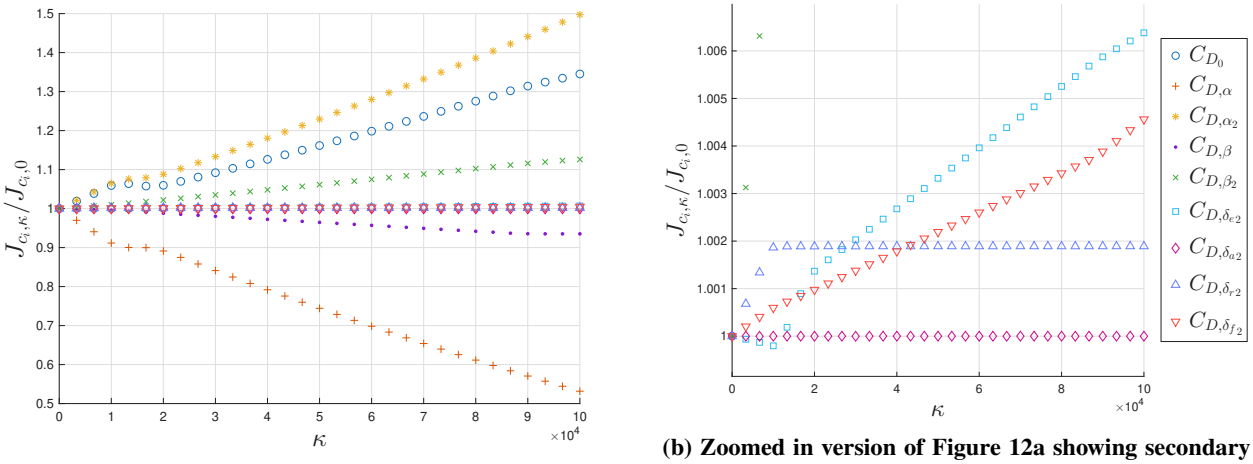


**(a) Primary variables cost function change with $\kappa$.**

**(b) Zoomed in version of Figure 12a showing secondary variables effect on the cost function change.**

**Fig. 12 Cost function change with sparsity parameter $\kappa$.**

Figure 12 shows that $C_{D_0}$, $C_{D,\alpha_2}$ and $C_{D,\beta_2}$ all exhibit increasing importance with higher levels of sparsity. $C_{D,\alpha}, C_{D,\beta}$ become decreasingly important with increasing levels of sparsity. This is due to the fact that these terms are small and that drag can be captured by the quadratic terms ($C_{D,\alpha_2}$, $C_{D,\beta_2}$). Of secondary importance, is the effect of $C_{D,\delta_{e2}}$, $C_{D,\delta_{f_2}}$. The effect of rudder and aileron on drag is minimal due to the lack of change in the cost function with increasing sparsity. Drag dependence on speed ($C_{D,V} = \frac{\partial C_D}{\partial V}$) as well as angular rates ($C_{D,p} = \frac{\partial C_D}{\partial p}$, $C_{D,q} = \frac{\partial C_D}{\partial q}, C_{D,r} = \frac{\partial C_D}{\partial r}$) were also investigated, however these terms were identified as zero.

## D. Drag System Identification Results

After identifying the dominant and non dominant terms in the postulated model, the least-squares linear algebra approach is used to solve for the parameters. The numerical results for a range of postulated models are shown in Table 7. The cost function $J_c^* = ||\boldsymbol{H}\boldsymbol{\theta}^* - \dot{\boldsymbol{E}}_s||_2$ is used as a metric to show the performance of the fit (square is removed for ease of comparison). Increasing the number of parameters was done in a stepwise fashion as proposed in [15]. This stepwise regression relies on selecting the subsequent parameter that decreases the cost function the most in the least-squares sense, indicated by $\Delta J_c$. The number in the top row in each of the parameter rows is the numerical value of that parameter for the stepwise iteration. The value in the bottom row corresponds to how much that parameter changes the cost function if added as a variable. Once a parameter is added, the parameter value is reported instead of $\Delta J_c$. The parameter uncertainty, $\sigma$, is reported for the final 7 parameter least-squares fit.

**Table 7 Parametric coefficient results using a different number of fitting variables in the least-squares solution. The computational drag estimates are from a wing-tail panel model developed in XFLR5. $C_{D_0}$ from computation has additions based on historical publications of [1, 22].**

| $C_i$ | $K=1$ | $K=2$ | $K=3$ | $K=4$ | $K=5$ | $K=6$ | $K=7$ | $\sigma_i$ | Computation |
|---|---|---|---|---|---|---|---|---|---|
| $J_c^*$ | 912.88 | 672.23 | 562.76 | 544.75 | 537.25 | 529.32 | 528.44 | NA | NA |
| $C_{D_0}$ | 0.05239 | 0.03798 | 0.03758 | 0.03554 | 0.03579 | 0.03725 | 0.0377 | 0.00179 | 0.0353 |
| $\Delta J_c$ | | | | | | | | | |
| $C_{D,\alpha}$ | | | | | | | -0.0323 | 0.00759 | 0 |
| $\Delta J_c$ | 161.01 | 0.5321 | 1.3175 | 1.975 | 0.8504 | 0.8858 | | | |
| $C_{D,\alpha_2}$ | | 1.5659 | 1.4632 | 1.4064 | 1.2681 | 1.2725 | 1.4139 | 0.0402 | 1.419 |
| $\Delta J_c$ | 240.64 | | | | | | | | |
| $C_{D,\beta}$ | | | | | | 0.0396 | 0.03696 | 0.00319 | 0 |
| $\Delta J_c$ | 0.3024 | 4.4201 | 0.2688 | 7.2798 | 7.9235 | | | | |
| $C_{D,\beta_2}$ | | | | 0.4266 | 0.4238 | 0.5602 | 0.5658 | 0.0250 | 0.088 |
| $\Delta J_c$ | 27.82 | 12.767 | 18.005 | | | | | | |
| $C_{D,\delta_{e2}}$ | | | | | 0.2096 | 0.2169 | 0.2035 | 0.0174 | 0.1363 |
| $\Delta J_c$ | 79.94 | 3.2428 | 7.5013 | 7.5032 | | | | | |
| $C_{D,\delta_{a2}}$ | | | | | | | | NA | 0.325 |
| $\Delta J_c$ | 0.6796 | 0.7120 | 1.4941 | 1.3385 | 1.3215 | 2.2832 | | | |
| $C_{D,\delta_{r2}}$ | | | | | | | | NA | 0.4583 |
| $\Delta J_c$ | 2.0195 | 2.203 | 3.3026 | 0.1495 | 1.532 | 0.1443 | | | |
| $C_{D,\delta_{f_2}}$ | | | 0.3819 | 0.3862 | 0.39273 | 0.3767 | 0.37744 | 0.00577 | 0.2457 |
| $\Delta J_c$ | 109.28 | 109.47 | | | | | | | |
| Variable to add | $C_{D,\alpha_2}$ | $C_{D,\delta_{f_2}}$ | $C_{D,\beta_2}$ | $C_{D,\delta_{e2}}$ | $C_{D,\beta}$ | $C_{D,\alpha}$ | stop | | |

The stepwise regression results in Table 7 reflect the model form study performed using the iterative convex solution. $C_{D_0}$, $C_{D,\alpha_2}$, $C_{D,\delta_{f_2}}$, $C_{D,\beta_2}$ all decrease the cost function significantly. $C_{D,\delta_{e2}} C_{D,\beta}, C_{D,\alpha}$ don't decrease the cost function as much but are identifiable. $C_{D,\alpha}$ was selected over $C_{D,\delta_{a2}}$ between the 6 to 7 least-squares iteration because the identified value of $C_{D,\delta_{a2}}$ was negative. The effect of aileron and rudder is either not significant or can't be identified with the available data. The lower variances of the identified model align with the dominant terms in the model form study. $C_{D_0}, C_{D,\alpha_2}, C_{D,\beta_2}, C_{D,\delta_{f_2}}$ are all important and have relatively small standard deviations (with respect to their nominal values). Furthermore, the flight identified value of $C_{D_0}, C_{D,\alpha}, C_{D,\alpha_2}$ and $C_{D,\delta_{e2}}$ are all within $3\sigma$ of the values estimated by computation. Because the aircraft's main wing has a symmetric airfoil cross section (NACA 0012), the drag polar is expected to be symmetric (with respect to $\alpha$) and thus $C_{D,\alpha}$ is expected to be zero [36]. The panel code does not model the effect of the fuselage and thus, $C_{D,\beta_2}$ is not captured well by computation.

### E. Verification

The identified thrust and drag model can be used to reconstruct energy maneuverability via the analytical form (right hand side of Equation 8). This reconstructed energy maneuverability state can be compared to the sensed energy maneuverability (Equation 7) to verify that the model:

1) fits the provided data used in system identification,
2) has predictive capability on portions of data that were not used in the system identification process.

Figure 13a shows energy maneuverability during a throttle doublet maneuver that was used in the system identification procedure. Figure 13b shows energy maneuverability of section of data that was not used in system identification. The measured or *exact* energy maneuverability (Equation 7) is compared to a numerically differentiated (using Euler's method) time history of the energy state of the aircraft ($E_s = h + V^2/2g$). The energy state of the aircraft is constructed using the n580 altitude and velocity solution. There are certain "blips" in the numerically differentiated specific energy

time history due to the discontinuity introduced by the GPS measurement update in the n580's Kalman Filter.

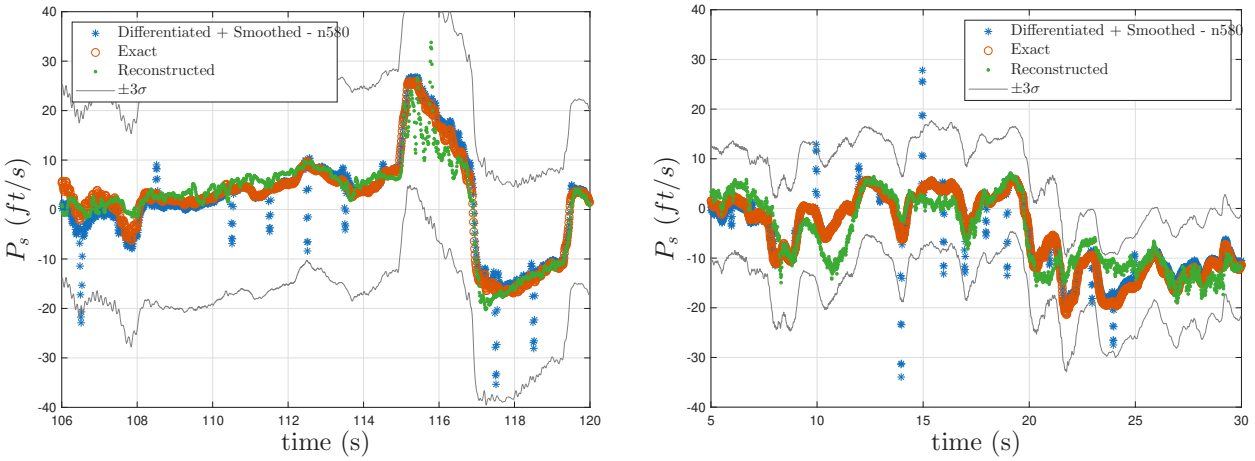


**(a) Throttle doublet used to identify the thrust model.** **(b) Verification data.**

**Fig. 13 Energy maneuverability time histories with $\pm 3\sigma$ bound.**

As shown in Figure 13, the differentiated, sensed, and reconstructed energy maneuverability all align well for the data provided and stay within the estimated $3\sigma$ bound (except for GPS correction points in the differentiated time history). Furthermore, the identified model, provides predictive capability on data that was not used in the system identification procedure further validating the model.

## V. Conclusion

A new method based on sensed energy maneuverability has shown to identify thrust and drag models in flight. Flight test results of a highly instrumented Ultra Stick remotely piloted aircraft were used to showcase this method. A model form study was performed using an iterative convex optimization method which helps to reveal the dominant terms in the model/data. Thrust was identified using a throttle doublet maneuver time history and then fixed to identify the remaining drag model. An uncertainty analysis was performed on the sensed energy maneuverability function by propagating the individual sensor uncertainties using a first order Taylor series. This analysis revealed that acceleration in the $x$ direction was found to drive the overall uncertainty in energy maneuverability. Of secondary importance were angle of attack and $z$ acceleration measurements. The identified thrust and drag model was found to match computational results from a blade-element code for thrust, and a panel code for drag.

Lessons learned that were emphasized in this work include:

1) Having multiple sources of air data information is valuable for verification and estimation of instrumentation and sensor bias errors in acceleration and pressure measurements.
2) In order to obtain a thrust model in flight for a fixed-pitch propeller driven aircraft, data is needed that spans a large range of advance ratios.
3) Vibrations from the motor, structure, or flight significantly increases the uncertainty in the identified model because sensed energy maneuverability is highly sensitive to acceleration measurements.

Thrust and drag are challenging models to find from flight test. Energy maneuverability has been shown to be an effective tool in finding these models. Future work could include fusing multiple sources of energy maneuverability measurements to lower the overall energy maneuverability uncertainty as well as, designing maneuvers to maximize energy maneuverability observability and minimize measurement noise.

## Acknowledgments

The authors gratefully acknowledge the support of Honeywell Aerospace for funding, as well as for the hardware contributions, including the donation of the n580 inertial measurement unit used in this work. The authors also thank Curt Olson and Sabrina Shrestha for their assistance during flight testing with IBIS. However, the views expressed in this paper are those of the authors and do not necessarily reflect the views of any organization or individual.

# Appendix

## A. Air Data Transformations

Because the probes that measure the air data angles are mounted at the wingtips, the air data angles measured correspond to the air data at the wingtips not the center of gravity of the aircraft [14]. The measured angles can be translated into associated angles at the the center of gravity. First the $u$ velocity measured from the pitot probe is estimated at the wingtip via:

$$u_{wt} = u_{pitot} + r(y_{pitot} - y_{wt}) - q(z_{pitot} - z_{wt}) \tag{36}$$

where $y_{pitot}, z_{pitot}$ and $y_{wt}, z_{wt}$ are the distances from the pitot and wing tip to the center of gravity. For the Ultra Stick these are $y_{pitot} = 23"$, $z_{pitot} = -2"$, $y_{wt} = -38.5"$, $z_{wt} = -2"$. Next the $u_{wt}$ velocity can be translated to the center of gravity via the expression:

$$u_{CG} = u_{wt} + ry_{wt} - qz_{wt}. \tag{37}$$

By using the definition of $v = u \tan \beta_f$ and $w = u \tan \alpha$, the aerodynamic angles can be solved for:

$$\begin{aligned} \tan \beta_{f_{CG}} &= \frac{1}{u_{CG}} \left( u_{wt} \tan \beta_{f_{wt}} + pz_{wt} - rx_{wt} \right) \\ \tan \alpha_{CG} &= \frac{1}{u_{CG}} \left( u_{wt} \tan \alpha_{wt} + qx_{wt} - py_{wt} \right). \end{aligned} \tag{38}$$

## B. Static Thrust

A challenge in finding a thrust model in flight is obtaining data at very low advance ratios. This corresponds to a flight condition of airspeed being low and RPM being high. The condition of $J = 0$ corresponds to static thrust ($C_{T_0}$). Data for this condition was obtained on the ground by building a thrust stand and running it in calm wind conditions (Figure 14b). The thrust stand was made out of 80/20 and had a compression load cell that was calibrated using a known weight. The propeller, electronic speed control, as well as batteries on the thrust stand are the same components as on the aircraft. The motor on the thrust stand is the Spektrum 6362-250 kv Brushless Outrunner Motor. A plot of the static trust coefficient vs RPM is shown in Figure 14a.

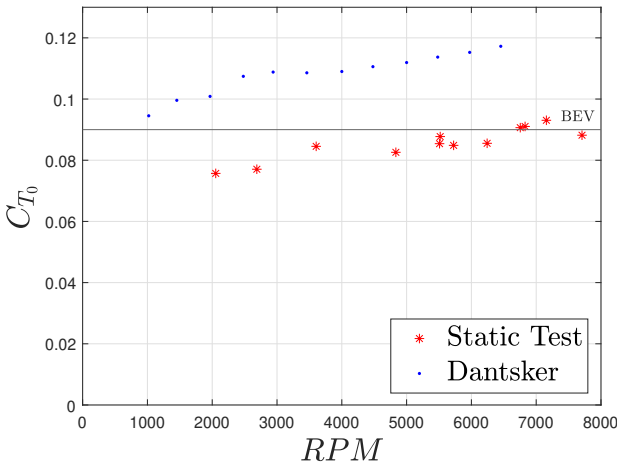


**(a) Static thrust coefficient versus $RPM$ comparison with [35].**

**(b) Thrust stand used to perform static thrust test.**

**Fig. 14 Static thrust coefficient and thrust stand.**

As shown in Figure 14a the static thrust coefficient obtained from the thrust stand data matches the computational estimate from blade-element-vortex theory. There is a mismatch between the published dataset [35] and the observed

experimental/computational data which could be due to installation effects and static thrust blade element modeling. Both the published and the thrust stand data exhibits RPM dependence. This trend is modeled as uncertainty in the thrust identification.

### C. Blade-Element Theory

Blade element theory is the most common approach to model propeller performance from first principles [4, 6]. The general approach is to split up the propeller blade up into a set of small spanwise sections and then model the loads of these sections in the thrust and torque directions. Then these loads can be integrated to obtain the overall thrust and power characteristics for a given propeller geometry and flight condition.

Critical to this theory is the accurate modeling of the two-dimensional cross sections of the propeller blade as well as the overall propeller geometry. The propeller geometry generally has a propeller pitch angle ($\beta$), airfoil chord length ($c$), and airfoil cross section as a function of radial coordinate $r$ (the propeller can also be swept but those effects are not investigated). Propeller pitch angle refers to the angle of twist or how the airfoil cross section is orientated with respect to the rotation plane. The geometry for the APC 16 × 8E propeller used by the Ultra Stick is shown in Figure 15. The 16 denotes a propeller diameter of 16 inches and a pitch of 8 inches.

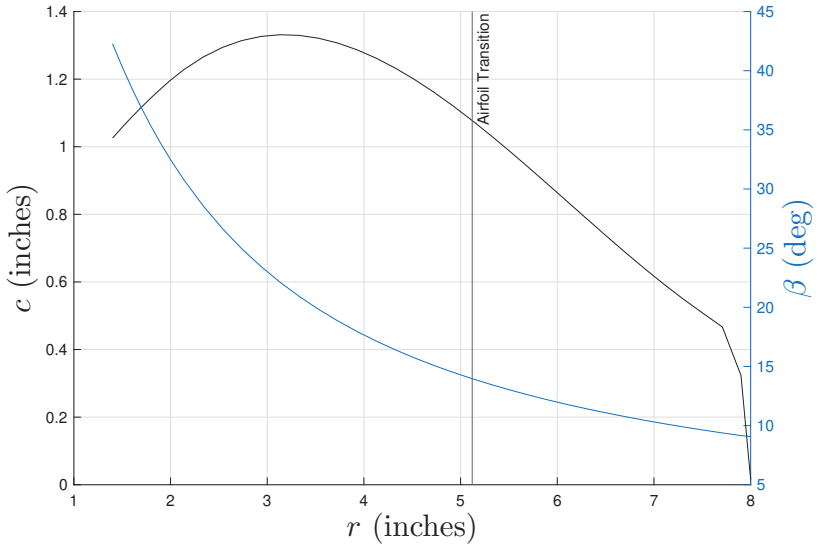


**Fig. 15 APC 16 × 8E propeller chord ($c$) and twist angle ($\beta$) as a function of radius. At $r = 5.12$ in the propeller cross section transitions from a E63 airfoil to a NACA 4412. Propeller geometry information was gathered from the APC propeller website.**

Geometry information by itself is not sufficient to close the loop and model the loads on the propeller. This is due to the fact the propeller has inflow and outflow conditions that are generated by its wake (or downwash). These inflow and outflow velocities modify the velocity vector seen by each of the propeller blade elements and thus the loads generated by them.

There are two general approaches which include momentum or vortex theory [37]. Momentum theory uses a streamtube to apply the law of conservation mass as well as momentum to close the set of equations [4, 38, 39]. Vortex theory uses Goldstein's Propeller Theory that models the vortex coming off of the tip of the propeller as a helix [4, 40]. Momentum theory has the deficiency that it cannot predict static thrust (upstream flow velocity becomes zero). Vortex theory doesn't have this deficiency. Both blade element momentum (BEM) as well as blade element vortex (BEV) codes have been developed and run on the APC 16 × 8E propeller's geometry. Airfoil cross section data was generated from XFOIL at a freestream $Re = 1e6$.

The lift and drag data for a two dimensional airfoil cross section needs to be corrected for a three dimensional rotating frame, hub and tip losses, as well as blended with a high angle of attack model. This rotating frame induces a Coriolis acceleration which enhances lift. A rotating frame correction factor presented in [41] is used to correct the two dimensional data. To model the tip and hub losses, or finite span effect of the propeller, another correction factor is used. These loss factors were originally proposed by Glauert in 1935 [42]. Besides the rotating frame as well as hub and

tip loss corrections, a high angle of attack model is needed as certain sections of the blade can be in the stall regime for normal operating conditions. Without applying some sort of stall correction to a linear low angle of attack model, certain portions of the blade will have very high loads and the integrated result will be inaccurate. A high angle of attack model from [43] is used in the blade element code.

### D. Drag Estimates from Historical References and Computational Aerodynamic Model

A panel model of the wing-tail was developed in XFLR5 which uses XFOIL [21] as the underlying modeling computational code. The main wing was modeled as a NACA 0012 airfoil and the tail surfaces were modeled as as a NACA 0005 with a rounded leading edge to approximate a flat plate. The panel model gridded $\alpha, \beta, V_\infty$ and solved for the resulting drag coefficient. First the drag coefficients dependence on speed was determined to be negligible.

The minimum drag coefficient varied from 0.0091 at a Reynolds number of 200,000 to 0.0062 at a Reynolds number of 1,000,000. After reviewing this data, a single speed of $V_\infty = 65\ ft/s$ was used to perform fits of $\alpha, \beta$ and control surface deflections. This speed was chosen as it is a representative speed for trim during takeoff and landing of IBIS. A fitted plot of $C_D$ versus $\alpha$ and $\beta$ (at zero control surface deflection) is shown in Figure 16.

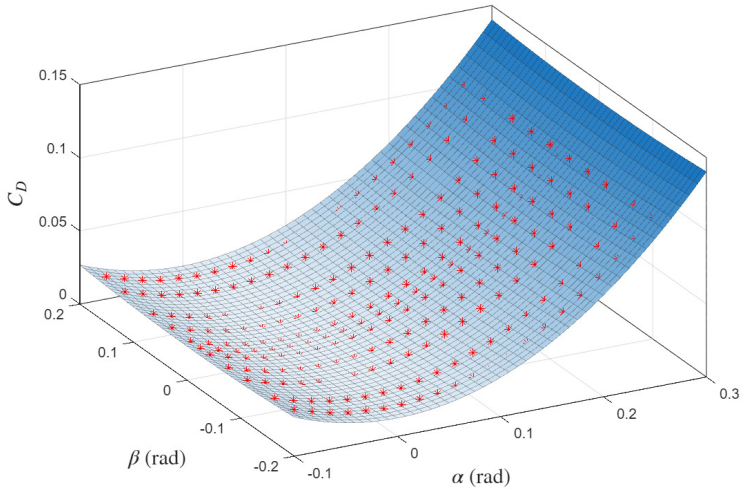


**Fig. 16 $C_D$ fit for $\alpha$ and $\beta$ at $V_\infty = 65\ ft/s$. This speed corresponds to a Reynolds number of $5 \cdot 10^5$ for the main wing of IBIS. The red data points correspond to data points generated by XFLR5 and the blue surface corresponds to a two dimensional polynomial fit in $\alpha, \beta$.**

After fitting drag coefficient with respect to $\alpha, \beta$ control surface deflections were fitted individually. After performing this study, the drag dependence exhibited purely quadratic behavior in all variables. This quadratic form was used to inform system identification.

While XFLR5 gives estimates for base drag for the wing and tail it does not include effects of interference drag, base drag from the fuselage, as well as landing gear. In order to get a better estimate of base drag, [1, 22] were used to add additional drag to the base drag estimated by XFLR5. The maximum base drag estimated by XFLR5 (minimum Reynolds number) was used as the numerical value for the wing tail drag.

The fuselage drag was estimated using [22] with a fuselage length to diameter ratio of $\frac{l_{fuselage}}{d_{fuselage}} = 10.4$ and a friction drag coefficient of $C_f = 0.005$ and using Equation 31 in [22]:

$$\frac{(C_{D_0})_{fuselage}}{C_f} = 3\left(\frac{l_{fuselage}}{d_{fuselage}}\right) + 4.5\left(\frac{l_{fuselage}}{d_{fuselage}}\right)^{1/2} + 21\left(\frac{l_{fuselage}}{d_{fuselage}}\right)^2. \tag{39}$$

The wing-tail interference drag was estimated from [22] using the fact that $D_{interference}/D_{section}$ varies between 3% and 13 % of base drag. The drag due to the landing gear was estimated from [1] using the bluff body drag at $Re = 7e4$, based on frontal wheel area. From all of these estimates, the total drag of the vehicle was summed up (normalizing with respect to a consistent reference area) using Equation 40:

**Table 8 Drag build up using historical references from [1, 22].**

| Item | $(C_D)_i$ | $\left(\frac{S_i}{S_w}\right)$ | $C_{D_i}$ | Reference |
|---|---|---|---|---|
| Wing - Tail | 0.009 | 1 | 0.009 | XFLR5 |
| Fuselage | 0.1639 | 0.0219 | 0.0036 | Hoerner (6-18, eqn. 31) |
| Tail Interference | $(C_{D_0})_{wing-tail}0.04$ | 1 | 0.00036 | Hoerner (8-12) |
| Wing Interference | 0.008 | 0.0219 | 0.000175 | Hoerner (8-18), high wing configuration |
| $2 \times$ Wheels | 1.1 | 0.0101 | 0.0222 | McCormick (Fig. 4.10) |

$$C_{D_0} = (C_{D_0})_{wing-tail} + (C_{D_0})_{fuselage}\left(\frac{S_{front}}{S_w}\right) + (C_{D_{interference}})_{tail} + (C_{D_{interference}})\left(\frac{S_{front}}{S_w}\right) + 2(C_{D_{wheel}})\left(\frac{S_{wheel}}{S_w}\right). \tag{40}$$

The total base drag of the vehicle was calculated to be $C_{D_0} = 0.0353$. This drag analysis neglects landing gear interference effects, GPS receiver drag, air data probe drag, and propeller slipstream effects. Furthermore induced drag is assumed to be primarily from the wing.

## References


[1] McCormick, B. W., *Aerodynamics, Aeronautics, and Flight Mechanics*, 2nd ed., John Wiley Sons, Inc., 1994.

[2] Vinh, N. X., *Flight Mechanics of High-Performance Aircraft*, 1st ed., Cambridge., 1993.

[3] Stengel, R., *Flight Dynamics*, 2nd ed., Princeton University Press, 2022.

[4] Phillips, W., *Mechanics of Flight*, 2nd ed., John Wiley Sons, Inc., Hoboken, New Jersey, 2010.

[5] Stevens, B., Lewis, F., and Johnson, E., *Aircraft Control and Simulation*, 3rd ed., Wiley, 2016.

[6] Ning, A., *Computational Aerodynamics*, BYU Course Notes, 2022.

[7] White, F., *Viscous Fluid Flow*, McGraw-Hill, 1991.

[8] Blazek, J., *Computational Fluid Dynamics Principles and Applications*, 3rd ed., Elsevier, 2005.

[9] Hoe, G., Owens, D. B., and Denham, C., "Forced Oscillation Wind Tunnel Testing for FASER Flight Research Aircraft," *AIAA Atmospheric Flight Mechanics Conference*, 2012. https://doi.org/10.2514/6.2012-4645.

[10] Drela, M., *Flight Vehicle Aerodynamics*, MIT Press, 2014.

[11] Kimberlin, R., *Flight Testing of Fixed-Wing Aircraft*, 1st ed., AIAA, Reston, VA, 2003.

[12] Rowse, J. H., "Propeller/Propfan In-Flight Thrust Determination," Tech. rep., Soceity of Automotive Engineers, 1993.

[13] Rogers, D. F., "Flight Determination of Partial-Span-Flap Parasite Drag With Flap Deflection," *Journal of Aircraft*, Vol. 47, No. 2, 2010, pp. 551–555. https://doi.org/10.2514/1.45654.

[14] Jategaonkar, R. V., *Flight Vehicle System Identification: A Time Domain Methodology*, 2nd ed., AIAA, Reston, VA, 2015.

[15] Morelli, E., and Klein, V., *Aircraft Systeim Identification: Theory and Practice*, 2nd ed., Sunflyte Enterprises, Williamsburt, VA, 2016.

[16] Tischler, M., and Remple, R., *Aircraft and Rotorcraft System Identification: Engineering Methods with Flight Test Examples*, 2nd ed., AIAA, Reston, VA, 2012.

[17] Boyd, J., Christie, T., and Gibson, J., "Energy-Maneuverability," *United States Air Force Report*, 1966. URL https://www.archives.gov/files/declassification/iscap/pdf/2011-052-doc1.pdf.

[18] Rutowski, E. S., "Energy Approach to the General Aircraft Performance Problem," *Journal of the Aeronautical Sciences*, Vol. 21, No. 3, 1954, p. 187–195. https://doi.org/10.2514/8.2956.

[19] Jaeger, S., and Hemati, M., "Hypersonic Glide Vehicle Trajectory Design using Constrained Energy Maneuverability," *AIAA Region V Student Conference*, 2025. https://doi.org/10.2514/6.2025-97945.

[20] Johnson, D. T., "Evaluation of Energy Maneuverability Procedures in Aircraft Flight Path Optimization and Performance Estimation," *United States Air Force Report*, 1972. URL https://apps.dtic.mil/sti/tr/pdf/AD0754909.pdf.

[21] Drela, M., "XFOIL: An Analysis and Design System for Low Reynolds Number Airfoils," *Low Reynolds Number Aerodynamics*, edited by T. J. Mueller, Springer Berlin Heidelberg, Berlin, Heidelberg, 1989, pp. 1–12.

[22] Hoerner, S. F., *Fluid-Dynamic Drag*, Hoerner Fluid Dynamics, 1965.

[23] Hemati, M., *Model Reduction and Approximation of Dynamical Systems*, University of Minnesota Course Notes, 2025.

[24] Boyd, S., and Vandenberghe, L., *Convex Optimization*, Cambridge, 2009.

[25] Simon, D., *Optimal State Estimation: Kalman, H Infinity, and Nonlinear Apporaches*, 1st ed., Wiley, 2006.

[26] Owens, B., Cox, D., and Morelli, E., "Development of a Low-Cost Sub-Scale Aircraft for Flight Research: The FASER Project," *25th AIAA Aerodynamic Measurement Technology and Ground Testing Conference*, 2006. https://doi.org/10.2514/6.2006-3306.

[27] Denham, C. L., and Owens, D. B., "Rotary Balance Wind Tunnel Testing for the FASER Flight Research Aircraft," *AIAA Atmospheric Flight Mechanics Conference*, 2016. https://doi.org/10.2514/6.2016-3105.

[28] Hamel, P. G., and Jategaonkar, R. V., "Evolution of Flight Vehicle System Identification," *Journal of Aircraft*, Vol. 33, No. 1, 1996, pp. 9–28. https://doi.org/10.2514/3.46898.

[29] Klein, V., "Estimation of Aircraft Aerodynamic Parameters from Flight Data," *Progress in Aerospace Sciences*, Vol. 26, No. 1, 1989, pp. 1–77. https://doi.org/https://doi.org/10.1016/0376-0421(89)90002-X.

[30] Morelli, E. A., "Estimating Noise Characteristics from Flight Test Data Using Optimal Fourier Smoothing," *Journal of Aircraft*, Vol. 32, No. 4, 1995, pp. 689–695. https://doi.org/10.2514/3.46778.

[31] Sama, M. P., Stombaugh, T. S., and Lumpp, J. E., "A Hardware Method for Time-Stamping Asynchronous Serial Data Streams Relative to GNSS Time," *Computers and electronics in agriculture*, Vol. 97, 2013, pp. 56–60.

[32] Erb, R., *Pitot-Statics and the Standard Atmosphere*, 5th ed., USAF Test Pilot School, 2021.

[33] Groves, P. D., *Principles of GNSS, Inertial, and Multisensor Integrated Navigation Systems*, 1st ed., Artech House, Boston, MA, 2008.

[34] Gebre-Egziabher, D., Bevly, D., and Petevello, M., *Integration of GNSS and INS: Part 1*, Artech House, Boston, MA, 2009.

[35] Dantsker, O. D., Caccamo, M., Deters, R. W., and Selig, M., "Performance Testing of APC Electric Fixed-Blade UAV Propellers," *AIAA AVIATION 2022 Forum*, 2022. https://doi.org/10.2514/6.2022-4020.

[36] Sachs, G., "Effect of Asymmetric Drag Polar Characteristics on Minimum Trimmed Drag," *Journal of Aircraft*, Vol. 17, No. 10, 1980, pp. 766–768. https://doi.org/10.2514/3.44685.

[37] Johnson, W., *Rotorcraft Aeromechanics*, Cambridge University Press, 2013.

[38] Ning, S. A., "A Simple Solution Method for the Blade Element Momentum Equations with Guaranteed Convergence," *Wind Energy*, Vol. 17, No. 9, 2014, pp. 1327–1345. https://doi.org/https://doi.org/10.1002/we.1636.

[39] Ning, A., "Using Blade Element Momentum Methods with Gradient-based Design Optimization," *Structural and Multidisciplinary Optimization*, Vol. 64, 2021, pp. 991–1014. https://doi.org/https://doi.org/10.1007/s00158-021-02883-6.

[40] Goldstein, S., "On the Vortex Theory of Screw Propellers," *Proceedings of the Royal Society of London. Series A, Containing Papers of a Mathematical and Physical Character*, Vol. 123, No. 792, 1929, pp. 440–465. https://doi.org/10.1098/rspa.1929.0078.

[41] Lindenburg, C., "Investigation into Rotor Blade Aerodynamics: Analysis of the Stationary Measurements on the UAE Pahse-VI Rotor in the NASA-Ames Wind Tunnel," *NREL Report*, 2003.

[42] Glauert, H., *Airplane Propellers*, Springer, 1935.

[43] Viterna, L. A., and Janetzke, D. C., "Theoretical and Experimental Power from Large Horizontal-Axis Wind Turbines," Tech. rep., NASA, Cleveland, OH (USA). Lewis Research Center, 09 1982. https://doi.org/10.2172/6763041.